Article

Dual-mode narrowband organic photodetectors for self-aligned imaging in NIR-I and NIR-II

Yu Tang [1], Zhuangmiao Wang [1], Mingsheng Gao [1], Jiayin Han [1], Leiming Yuan [1,2] & Furong Zhu [1] ✉

The ability to detect and image in the near-infrared (NIR) regions, specifically NIR-I (700–900 nm) and NIR-II (1000–1700 nm), is crucial for medical diagnostics and bioimaging due to their exceptional tissue penetration and absorption characteristics. Organic photodetectors (OPDs) present a promising solution for self-aligned imaging in these regions, due to their tunable optoelectronic properties and flexible fabrication processes. However, achieving high-performance dual-mode narrowband OPDs for NIR-I and NIR-II detection remains a significant challenge due to the inherently broadband nature of most organic semiconductor materials. In this study, we introduce a bias-switchable dual-mode narrowband OPD with a back-to-back stacked charge collection narrowing/photodiode-type double bulk heterojunction (BHJ) architecture. The dual-mode narrowband OPD exhibits excellent wavelength selectivity and enhanced imaging capabilities, facilitating self-aligned imaging in both NIR-I and NIR-II regions. Additionally, the double BHJ architecture provides design flexibility, allowing for the realization of dual-mode narrowband responses through various BHJ configurations.

Detection and imaging of both near-infrared (NIR)-I (700-900 nm) and NIR-II (1000-1700 nm) electromagnetic waves play significant roles in medical diagnostics, therapeutic monitoring, and various industrial applications, due to their properties in tissue penetration, scattering, and absorption[1–5]. Inorganic semiconductor, e.g., silicon and III-V compound semiconductors, based photodetectors are broadband which require dedicated appropriate bandpass filters to achieve the desired spectral response. The rigidity of these filters and the challenges associated with assembling small-size optical units limit their application in flexible or high-resolution conformal optical devices. The use of bandpass filters decreases the overall radiometric performance, increases device integration complexity, and raises fabrication costs. Emerging organic photodetectors (OPDs) are promising photodetector technology. They offer additional advantages including huge material varieties with tunable optoelectronic properties and solution-fabrication processes that are capable of use in curved image sensors, enhanced NIR responses, large areas, and flexible devices[6–9]. Various solutions have been proposed to develop different OPDs for achieving spectral selective detection, such as filter-free[10–12], microcavity structures[13–18], narrowband absorbing materials, charge injection narrowing[19,20], exciton dissociation narrowing[21] and charge collection narrowing (CCN) methods[22,23]. Although these approaches improve the performance of single-band OPDs, they do not facilitate multispectral light detection.

Bias-switchable dual-band OPDs offer capabilities that surpass those of single-band OPDs. Various methods have been explored to realize dual-band detection[24–26]. For instance, a bias-controllable short-wave infrared (SWIR) and middle-wave infrared (MWIR) dual-band detector, prepared using stacked mercury telluride quantum dots (QDs) junctions, has been reported[27]. This QD-based dual-band photodetector, however, suffers from significant spectral crosstalk between its SWIR and MWIR responses due to the overlap in the

[1]Department of Physics, Research Centre of Excellence for Organic Electronics and Institute of Advanced Materials, Hong Kong Baptist University, Kowloon Tong, Hong Kong, China. [2]College of Electrical and Electronic Engineering, Wenzhou University, Wenzhou, China. ✉e-mail: frzhu@hkbu.edu.hk

absorption spectra of different-sized mercury telluride QDs. In previous work, we developed a bias-controllable dual-band OPD comprising a visible-light-absorbing layer/optical spacer/NIR-light-absorbing layer-based trilayer photomultiplication (PM) structure[28]. An NIR-induced photocurrent is generated by enhanced charge injection via a tunneling effect at the metal interface with the NIR-absorbing layer when operated under a reverse bias. The trilayer PM-OPD responds to visible light under a forward bias, enabled by enhanced charge injection at its front contact with the visible-light-absorbing layer. These two operating conditions provide the trilayer PM-OPD with dual-band sensing capabilities for NIR and visible light.

In general, the spectral responses of the photodetectors are determined by the absorption of the active materials and optical profile in the devices. Many progress has been made in the development of broadband OPDs. In the practical application, visualization of NIR-I and NIR-II is critical for bioimaging analysis[29–31]. However, the reports on dual-mode narrowband OPDs for NIR-I and NIR-II detection are rather rare. It is a great challenge to achieve high-performance NIR-I and NIR-II dual-mode narrowband OPDs. In this work, we present the results of our research on developing a back-to-back stacked CCN/photodiode double bulk heterojunction (BHJ) OPD for spectrally selective response in NIR-I and NIR-II, as illustrated in Fig. 1a. The back-to-back double BHJ configuration offers significant design flexibility and process versatility, enabling various double BHJ combinations. For instance, an NIR-I narrowband spectral response can be achieved using a 3.5 μm thick front CCN junction, comprising a binary blend layer of poly[(2,6-(4,8-bis(5-(2-ethylhexyl-3-fluoro)thiophen-2-yl)-benzo[1,2-b:4,5-b']dithiophene)) -alt-(5,5-(1',3'-di-2-thienyl-5',7'-bis(2-ethylhexyl) benzo[1',2'-c:4',5'-'] dithiophene-4,8-dione)] (PM6): 3,9-bis(2-methylene-((3-(1,1-dicyanomethylene)-6,7-difluoro)-indanone))-5,5,11,11-tetrakis(4-hexylphenyl)-dithieno[2,3-d:2',3'-d']-s-indaceno [1,2- b:5,6-b'] dithiophene (IT-4F) (1:1), in the double BHJ heterojunction OPD. The rear BHJ can utilize various blend systems of low bandgap polymers and nonfullerene acceptors with absorption extending into the NIR-II range. By adjusting the difference in absorption edges between the front and rear junctions, a narrowband spectral response in the NIR-II can be realized.

Our results demonstrate that dual-mode narrowband spectral responses in the NIR-I and NIR-II can be effectively achieved by adjusting the biases across the OPD, comprising a back-to-back stacked PM6:IT-4F-based CCN front junction and a rear long-wavelength light absorbing ternary BHJ of poly[4,8-bis(5-(2-ethylhexyl)thiophen-2-yl)benzo[1,2-b;4,5-b']dithiophene-2,6-diyl-alt-(4-(2-ethylhexyl)-3-fluorothieno[3,4-b]thiophene-)-2-carboxylate-2-6-diyl] (PTB7-Th), 2,2'-((2Z,2'Z)-((5,5'-(4,4-bis(2-ethylhexyl)-4H-cyclopenta[1,2-b:5,4-b'] dithioph-ene-2,6-diyl) bis((4-(2-ethylhexyl)oxy) thiophene-5,2-diyl)) bis(methanylylidene)) bis (5,6-dichloro -3-oxo-2,3-dihydro-1H-indene-2,1-diylidene))dimalononitrile (COTIC-4Cl), and 2,2'-((2Z,2'Z)-((12,13-Bis(2-ethylhexyl)-3,9-diundecyl-12,13-dihydro-[1,2,5]thiadiazolo [3,4-e]thieno[2",3":4', 5'] thieno [2',3':4,5] pyrrolo [3,2-g]thieno[2',3':4,5]thieno[3,2-b]indole-2,10-diyl)bis (methanylylidene))bis(5,6-difluoro-3-oxo-2,3-dihydro-1H-inde (Y6). The performance of the NIR-I/NIR-II dual-mode narrowband OPDs, including photoresponsivity, noise current, and specific detectivity, $D^*(\lambda)$, was analyzed. The CCN/photodiode-type dual-mode narrowband OPDs exhibit excellent spectral selective detection, enabling self-aligned imaging analysis in distinct bands through the combination of different BHJ configurations.

Results and discussion

The schematic cross-sectional view of the double BHJ OPD, comprising a layer configuration of glass/ITO/ZnO (10 nm)/PM6:IT-4F (1:1) (3.5 μm)/MoO$_3$ (5 nm)/PTB7-Th:COTIC-4Cl:Y6 (1:1.05:0.45) (670 nm)/ZnO (10 nm)/Ag, is shown in Fig. 1a. In this device structure, the front 3.5 μm thick PM6:IT-4F (1:1)-based photoactive layer functions as a CCN junction responding for the NIR-I light, and a 670 nm thick rear PTB7-Th:COTIC-4Cl:Y6 (1:1.05:0.45)-based photoactive layer is responsible for spectral response at NIR-II range. A 5 nm thick MoO$_3$ interlayer acts as a common anode connecting the front and rear photoactive layers forming a back-to-back CCN/photodiode type double heterojunction structure. The selection of the thicknesses of both junctions was guided by optical simulation to optimize the absorption distribution in the double BHJ OPD, taking advantage of the complementary absorption characteristics of PM6:IT-4F (1:1)-based CCN and PTB7-Th:COTIC-4Cl:Y6 BHJ layers, as shown in Fig.1b. This enables the enhanced spectral selective narrowband detection for NIR-I through CCN effect of the front PM6:IT-4F junction, and the built-in filtering effect of the front PM6:IT-4F photoactive layer for narrowband NIR-II detection by the PTB7-Th:COTIC-4Cl:Y6-based rear BHJ. The molecular structure and schematic energy level diagram of the function materials used in this work are shown in Supplementary Fig. 1 and Supplementary Fig. 2.

The profile of the absorption distribution in PM6:IT-4F/MoO$_3$/PTB7-Th:COTIC-4Cl:Y6-based NIR-I and NIR-II dual-mode narrowband OPD was analyzed. The optical simulation reveals clearly that the incoming light with a portion over the wavelength range from 400 to 800 nm can be fully absorbed by the PM6:IT-4F-based front junction with a layer thickness of >1.0 μm, enabling for a narrowband spectral response in NIR-I band due to the CCN effect. Whereas the longer wavelength part of the incoming light with the wavelengths above
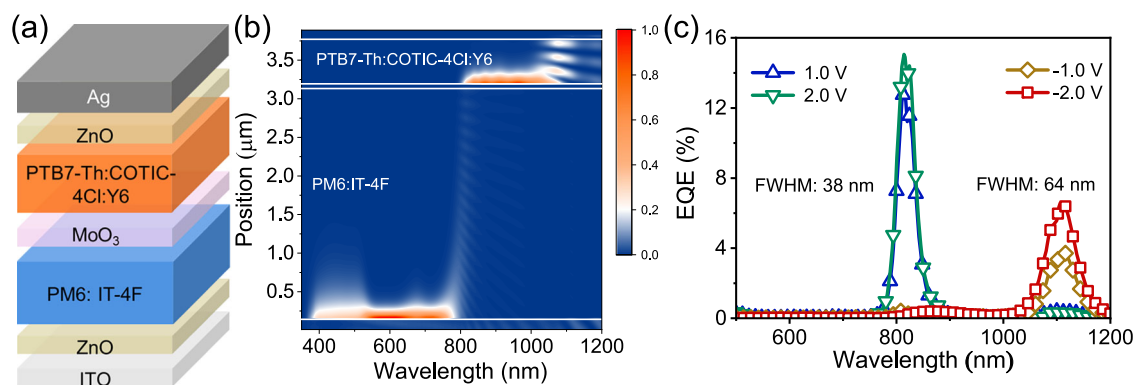
Fig. 1 | Dual-mode narrowband OPD. a Schematic cross-sectional view and **b** absorption profile of the dual-mode narrowband OPD, comprising a layer configuration of glass/ITO/ZnO (10 nm)/PM6:IT-4F (1:1) (3.5 μm)/MoO$_3$ (5 nm)/PTB7-Th:COTIC-4Cl:Y6 (1:1.05:0.45) (670 nm)/ZnO (10 nm)/Ag. **c** *EQE* spectra measured for the OPD operated under forward biases of 1.0 and 2.0 V, showing a narrowband spectral response in the NIR-I range, with a peak wavelength of 814 nm, and the ones measured for the OPD operated under reverse biases of −1.0 and −2.0 V, showing a narrowband spectral response in the NIR-II range, with a peak wavelength of 1108 nm.

800 nm can penetrate the front PM6:IT-4F-based front junction and be absorbed by the rear PTB7-Th:COTIC-4Cl:Y6 photoactive layer, enabling for a narrowband spectral response in NIR-II band, due to the difference in absorption edges between the PM6:IT-4F-based CCN junction and the rear PTB7-Th:COTIC-4Cl:Y6-based BHJ, as shown in Fig. 1b. An NIR-I narrowband spectral response is clearly demonstrated when the OPD is operated under a forward bias, and an NIR-II narrowband spectral response is observed when the OPD is operated under a reverse bias. A narrowband spectral response in the NIR-I range with a peak wavelength of 814 nm and full width at half maximum (FWHM) of 40 nm and 38 nm is observed for the dual-mode narrowband OPD operated at 1.0 and 2.0 V, respectively. A narrowband spectral response in the NIR-II range with a peak wavelength of 1108 nm and FWHM of 63 nm and 64 nm is observed for the OPD operated under reverse biases of −1.0 and −2.0 V, respectively, as shown in Fig. 1c. *EQE* of the OPD can be expressed using the following expression[32]:

$$EQE(\lambda) = \eta_{abs}(\lambda) \cdot IQE(\lambda) \tag{1}$$

where the $\eta_{abs}(\lambda)$ is the light absorption efficiency of the photoactive layer, and the internal quantum efficiency, $IQE(\lambda)$, is the ratio of photogenerated charges to the absorbed photons, which is strongly related to the absorbing nature of materials. A possible path to achieve narrowband photoresponse is to use a photoactive material with narrowband absorption feature. However, most of the organic semiconductor materials including the polymers and acceptors used in this work, are broadband absorbers. Realization of the dual-mode narrowband spectral response in OPDs prepared using the broadband absorbers requires dedicated device engineering.

The optical simulation reveals that photons with longer wavelengths have a deeper penetration depth, so that they have a longer penetration path. The organic semiconductor materials usually have a high absorption over the visible wavelength range and have a relatively weaker absorption near their band tail because of the energy band structure. A few hundred nanometer thick photoactive layer in an OPD generally possesses a broadband absorption and nearly uniform optical distribution across the layer. However, as the layer thickness increases, narrowband absorption behavior occurs as only those long path penetration photons with energy approaching the band edge can reach to the rear side of the photoactive layer, revealing a narrowband absorption behavior as seen in the CCN effect. The profile of the absorption distribution in a discrete OPD of a glass/ITO/ZnO/PM6:IT-4F (1:1)/MoO$_3$/Ag is shown in Supplementary Fig. 3. As the thickness of the front PM6:IT-4F-based photoactive layer increases, the spectral absorption gradually changes from its broadband absorption to a narrowband spectral response, the photogenerated charges generated by the short-wavelength photons loss to the recombination and do not contribute to the photocurrent due to the CCN effect[33–35]. *EQE* spectra measured for the PM6:IT-4F (1:1)-based discrete OPD clearly reveal the charge collection narrowing effect when the BHJ layer varies over the thickness range from 0.7 to 3.5 μm, as shown in Supplementary Fig. 4.

The light absorption in the photoactive layer is dependent on the wavelength of incoming light and the optical profile in the film. Schematic diagrams illustrating the spectral selective responses of the dual-mode narrowband OPD are shown in Fig. 2. When the dual-mode narrowband OPD is operated under forward bias, as shown in Fig. 2a, the rear PTB7-Th:COTIC-4Cl:Y6-based junction is under its forward conduction status with a small voltage drop, while the front PM6:IT-4F-based CCN junction is under its detection mode, as only photons with wavelengths near the absorption edge of the PM6:IT-4F-based CCN junction can be detected, realizing an NIR-I narrowband spectral response. When the dual-mode narrowband OPD is operated under reverse bias, as shown in Fig. 2b, the front PM6:IT-4F-based CCN junction is under its conduction mode with a low voltage drop, the rear
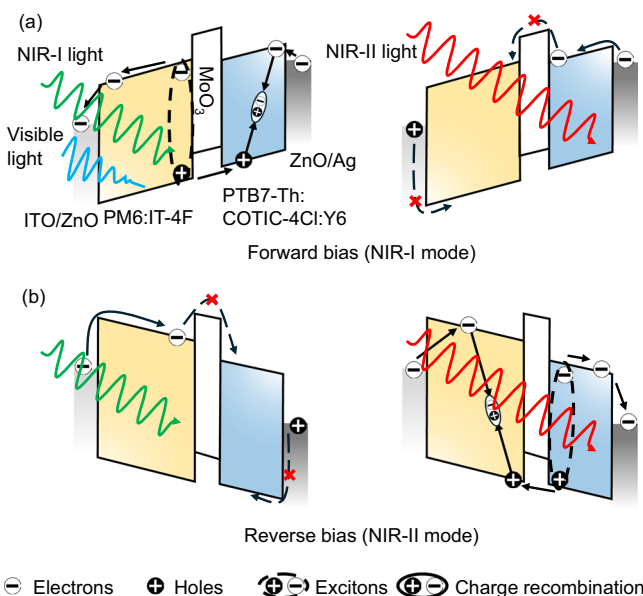
Fig. 2 | Spectral selective responses. Schematic diagrams illustrate the spectral selective responses of the dual-mode narrowband OPD: **a** under forward bias, with the front junction responding to the short wavelength part of the incoming light, and **b** under reverse bias, with the rear junction responding to the long wavelength part of the incoming light.

PTB7-Th:COTIC-4Cl:Y6-based BHJ is then under its detection mode. It responds to longer-wavelength photons that pass through the front junction, producing a narrowband spectral response in the NIR-II range, due to the difference in the absorption edges of the front and rear junctions in the double BHJ OPD.

The photoresponsivity, $R(\lambda)$, and the specific detectivity, $D^*(\lambda)$, of the dual-mode narrowband OPD are calculated using the following formula:
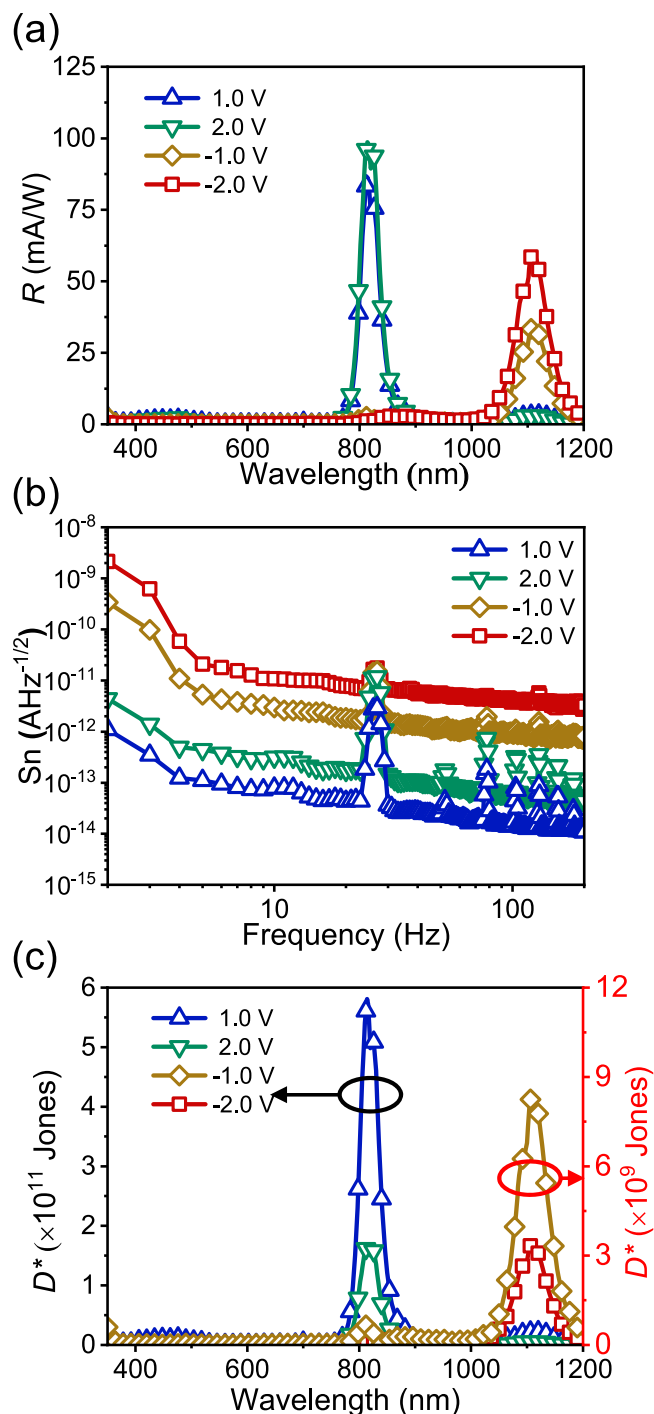
$$R(\lambda) = EQE \times \frac{q\lambda}{hc} \tag{2}$$

$$D^*(\lambda) = \frac{R\sqrt{A}}{S_n} \tag{3}$$

where q is the elementary charge, λ is the wavelength of the incident light, h is the Planck constant, c is the speed of light in vacuum, A is the active area in cm^2, S_n is the noise spectral density of the device measured in the dark[36,37]. Under a forward bias, the OPD shows narrowband behavior with a maxima $R(\lambda)$ of 100 mA/W at the peak wavelength of 814 nm. $R(\lambda)$ of 50 mA/W at 1108 nm was observed for the dual-mode narrowband OPD operated under a reverse bias, as shown in Fig. 3a. The $R(\lambda)$ increases with the applied bias, because of a higher internal field across the device that facilitates the swap out of the photogenerated charges. The noise current includes the shot noise (i_{shot}), thermal noise ($i_{thermal}$), 1/f noise ($i_{1/f}$), and generation-recombination noise (i_{g-r}) and can be described below:

$$S_n = \sqrt{i_{shot}^2 + i_{thermal}^2 + i_{1/f}^2 + i_{g-r}^2} \tag{4}$$

$$i_{shot} = \sqrt{2q \times I_D \times B} \tag{5}$$

$$i_{thermal} = \sqrt{\frac{4kTB}{R_{sh}}} \tag{6}$$

Fig. 3 | NIR-I and NIR-II dual-mode narrowband OPD. a Photoresponsivity, $R(\lambda)$, **b** noise spectral density, S_n, and **c** the specific detectivity, $D^*(\lambda)$ measured for the NIR-I and NIR-II dual-mode narrowband OPD, operated under forward biases of 1.0 and 2.0 V, and reverse biases of −1.0 and −2.0 V.

electron injection in the OPD, from Ag side, is significantly influenced by the forward bias. Under reverse bias, frequency dominated noise current indicates the intensive trap and de-trap process introduced by the fabrication process. The lower dark current in the OPD, operated under forward bias, is closely related to a 3.5 μm thick front PM6:IT-4F layer, as compared to the relatively thinner PTB7-Th:COTIC-4Cl:Y6 layer (670 nm). Overall, an S_n of 4.4×10^{-14} A/Hz$^{1/2}$ was obtained for the dual-mode narrowband OPD operated under a forward bias of 1.0 V, and an S_n of 1.2×10^{-12} A/Hz$^{1/2}$ is obtained for the dual-mode narrowband OPD operated under a reverse bias of −1.0 V at the frequency of 100 Hz. A D^* of 6.0×10^{11} Jones was obtained for the narrowband spectral response in the NIR-I (780–900 nm) range when the dual-mode narrowband OPD is operated under a forward bias, and a D^* of 8.0×10^9 Jones was obtained for the narrowband response in the NIR-II (1000–1200 nm) region when the OPD is operated under a reverse bias, as shown in Fig. 3c.

The spectral rejection ratio (*SRR*) of the NIR-I and NIR-II dual-mode narrowband OPD is analyzed. *SRR* is the ratio of responsivity at the target wavelength to the untargeted wavelength described by following expression[12]:
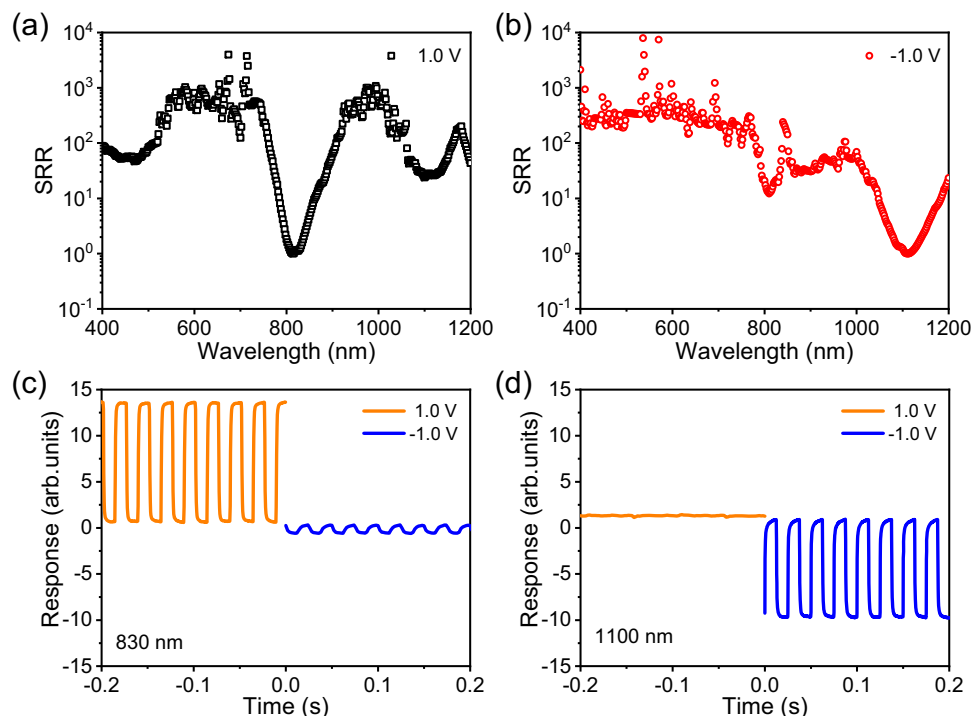
$$SRR(\lambda_{target}, \lambda_{ref}) = \frac{R(\lambda_{target})}{R(\lambda_{ref})} \qquad (7)$$

where the $R(\lambda_{target})$ is the photoresponsivity measured for the OPD in the targeting wavelength range, the $R(\lambda_{ref})$ is the responsivity out of the detection wavelength range. *SRR* calculated for the NIR-I and NIR-II dual-mode narrowband OPD, with the configuration of glass/ITO/ZnO (10 nm)/PM6:IT-4F (1:1) (3.5 μm)/MoO$_3$ (5 nm)/PTB7-Th:COTIC-4Cl:Y6 (1:1.05:0.45) (670 nm)/ZnO (10 nm)/Ag, operated under a forward bias of 1.0 V and a reverse bias of −1.0 V are shown in Fig. 4a and b. At the NIR-I detection mode, a high *SRR* of 1027 was obtained at the wavelength of 580 nm, revealing a low crosstalk at the visible regime due to the CCN effect. The current density–voltage (*J–V*) characteristics, measured for the NIR-I and NIR-II dual-mode narrowband OPD in the dark, under illumination of an 830 nm LED light source and a 1100 nm LED light source, are shown in Supplementary Fig. 5a and b. A dynamic range (DR) of 85 dB for NIR-I (830 nm) is achieved for the dual-mode narrowband OPD operated under a forward bias of 3.0 V, and a similar DR of 83 dB in NIR-II (1100 nm) is obtained for the dual-mode narrowband OPD operated under a reverse bias of −3.0 V, as shown in Supplementary Fig. 5c and d.

The response time of the dual-mode narrowband OPD was examined by recording the time that the photocurrent changes from the 10% to 90 % for rise time (τ_r) and 90 % to 10 % for fall time (τ_f)[42]. The response time of the NIR-I and NIR-II dual-mode narrowband OPD operated under a forward bias of 1.0 V and a reverse bias of −1.0 V was examined using illumination of an NIR-I (830 nm) LED source and an NIR-II (1100 nm) LED light source. The dual-mode narrowband OPD has a rise time of 1.4 ms and a fall time of 1.1 ms when it is operated under a forward bias of 1.0 V for detecting the NIR-I light, as shown in Supplementary Fig. 6. The dual-mode narrowband OPD has a rise time of 1.4 ms and fall time of 1.5 ms when it is operated under a reverse bias of −1.0 V for detecting NIR-II light. The slower response time, observed for the dual-mode narrowband OPD operated under forward bias, is related to the increased charge transfer processes in the thick CCN photoactive layer, leading to an f_{-3dB} of 0.7 kHz for the dual-mode narrowband OPD operated under a forward bias of 1.0 V, and an f_{-3dB} of 1.1 kHz for the OPD operated under a reverse bias of −1.0 V, as shown in Supplementary Fig. 7.

Transient photoresponse measured for the NIR-I and NIR-II dual-mode narrowband OPD operated at 1.0 and −1.0 V, under illumination of an NIR-I (830 nm) LED light source and an NIR-II (1100 nm) LED light source is shown in Fig. 4c and d. Under illumination of an 830 nm LED light source, the dual-mode narrowband OPD, operated under

where I_D is the dark current, B is the measurement bandwidth, k is the Boltzmann constant, and R_{sh} is the shunt resistance. The i_{sho} is determined by the charge injection and $i_{thermal}$ is caused by the thermal excitation[38]. The i_{shot} and the $i_{thermal}$ are considered as the main sources of the noise current in OPDs, which is independent of frequency. On the contrary, the 1/f noise and i_{g-r} depend on the frequency, they become the kay noise factor in an OPD operated under high biases[39–41]. S_n results measured for the dual-mode narrowband OPD operated under different forward and reverse biases are shown in Fig. 3b. The

Fig. 4 | Bias-switchable dual-mode narrowband OPD. *SRR* calculated for the NIR-I and NIR-II dual-mode narrowband OPD operated under **a** a forward bias of 1.0 V and **b** a reverse bias of −1.0 V. Transient photoresponse measured for the dual-mode narrowband OPD operated at 1.0 V and −1.0 V, under illumination of **c** an NIR-I (830 nm) LED light source and **d** an NIR-II (1100 nm) LED light source.

forward bias, has a strong spectral response to the NIR-I light. Whereas it has a very weak response to NIR-I light when the OPD is operated under reverse bias. When the dual-mode narrowband OPD was exposed to a 1100 nm LED light source and operated under a reverse bias of −1.0 V, an obvious photoresponse was observed. On the contrary, a weak spectral response to NIR-II light was seen when the OPD was operated under a forward bias of 1.0 V. The dual-mode narrowband OPD reveals the clear NIR-I (830 nm) and NIR-II (1100 nm) narrowband spectral selective responses, depending on the polarity of the bias applied across the device. The CCN/photodiode-type dual-mode narrowband OPD offers device design freedom and fabrication flexibility, enabling spectral selective detection across distinct bands by utilizing various BHJ combinations. For example, the bias-switchable dual-NIR narrowband spectral responses of a CCN/photodiode-type OPD with a combination of a PM6:Y6 (1:1.2)-based CCN junction, prepared using a precursor solution with a weight ratio of PM6 to Y6 of 1:1.2, and a PTB7-Th:COTIC-4Cl:Y6 (1:1.05:0.45)-based photodiode junction, were examined. The dual-mode narrowband spectral response in the NIR region, having a peak wavelength of 900 nm and an FWHM of 46 nm, is clearly seen when the PM6:Y6/PTB7-Th:COTIC-4Cl:Y6-based dual-mode narrowband OPD is operated under a forward bias of 3.0 V. Similarly, a narrowband spectral response in the NIR-II region, having a peak wavelength of 1100 nm and an FWHM of 62 nm, is achieved when it is operated under a reverse bias of −3.0 V, as shown in Fig. 5a. We also examined the spectral selective photoresponses of the dual-mode narrowband OPD that are operated at a forward bias and a reverse bias, under illumination of an NIR-I (910 nm) LED light source and an NIR-II (1200 nm) LED light source. The results are shown in Supplementary Fig. 8.

The spectral crosstalk, $C_{V_2}^{V_1}$, of the dual-band narrowband OPDs was examined by analyzing the overlap in their spectral responses. This overlap reflects the spectral selective detection capability, which occurs when detecting electromagnetic waves in one band that include an undesired photocurrent contribution from light in another band.

$C_{V_2}^{V_1}$ can be calculated using the following expression[26]:

$$C_{V_2}^{V_1} = -20 \times \left| \log \frac{R(\lambda, V_1)}{R(\lambda, V_2)} \right| \tag{8}$$

where $R(\lambda, V_1)$ and $R(\lambda, V_2)$ are the responsivities of the OPD measured under different operating voltages, such as a forward bias of 3.0 V and a reverse bias of −3.0 V, at the wavelength λ. Figure 5b shows the wavelength-dependent spectral crosstalk of the dual-NIR narrowband OPD over a broad wavelength range covering visible light and NIR light. The results clearly show that the dual NIR narrowband OPD exhibits negligible wavelength-dependent spectral crosstalk over the NIR ranges when operated under different biases of 3.0 V and −3.0 V. A $C_{3.0V}^{-3.0V}$ of >−30 dB is obtained for the dual-NIR narrowband OPD, demonstrating its clear spectral selective narrowband detection capability.

An imaging measurement setup, as shown in Fig. 6a, was used to demonstrate the capabilities of self-aligned image analysis in NIR-I and NIR-II using the dual-mode narrowband OPD. An image was taken of the HKBU mask, with its upper part (e.g., the letters HK) covered by a 1000 nm bandpass filter, as shown in Fig. 6b. The HKBU mask is exposed to the incoming light covering wavelengths of NIR-I and NIR-II ranges. When the dual-mode narrowband OPD is operated under a forward bias of 1.0 V, it is in its NIR-I detection mode, e.g., responses to 810 nm part of the incoming light. Only BU part of the mask can be detected by the OPD in its NIR-I mode, although the 1100 nm part of the incoming light passes through the 1000 nm bandpass filter, but it cannot be detected by the OPD. Therefore, an image for the part of the mask not covered by the 1000 nm bandpass filter (i.e., the letters BU) can be produced by the dual-mode narrowband OPD operated under forward bias. When a reverse bias of −1.0 V is applied to the dual-mode narrowband OPD, it operates in its NIR-II detection mode. In this mode, the entire HKBU image can be produced, as shown in Fig. 6c. This is because the dual-mode narrowband OPD has a high spectral response
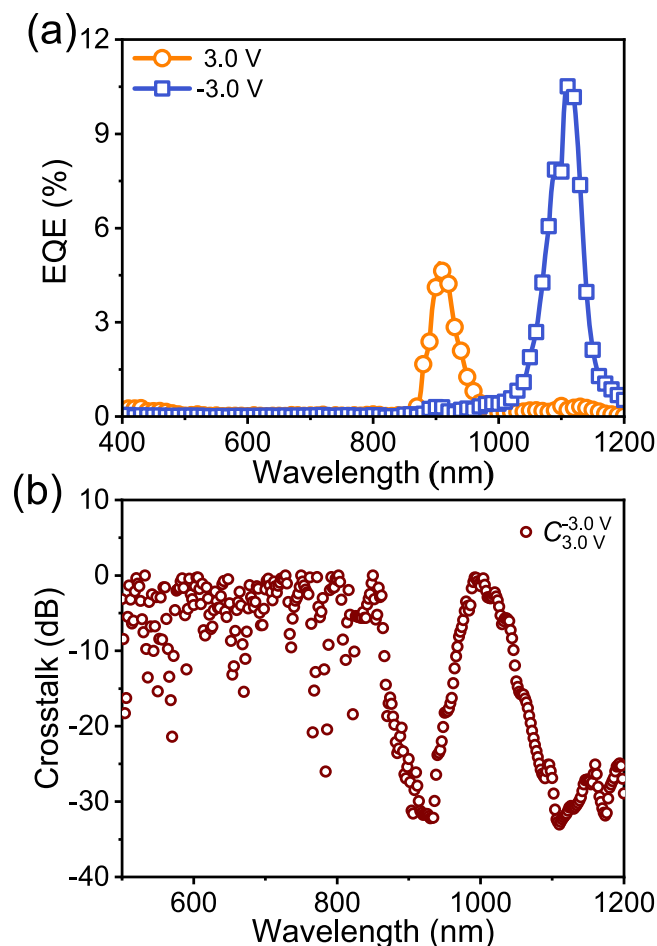
Fig. 5 | Characteristics of the dual-mode narrowband OPD. a *EQE* and **b** $C_{3.0V}^{-3.0V}$ obtained for a dual-mode narrowband OPD, made with a double BHJ layer configuration of glass/ITO/ZnO/PM6:Y6 (1:1)/MoO$_3$/PTB7-Th:COTIC−4Cl:Y6 (1:1.05:0.45)/ZnO/Ag.

to the 1100 nm part of the incoming light, which is exposed to both the covered and uncovered regions of the HKBU mask. The results reveal the advantages of the dual-mode narrowband OPD for use in self-aligned imaging analyses in NIR-I and NIR-II. The demonstrated performance underscores the potential of this technology for a wide range of imaging analyses in distinct bands.

Currently, the performance of dual-mode narrowband OPDs with spectral selective detection over broad wavelength ranges, such as short wavelength/long wavelength visible light range and visible/NIR, has been reported. However, reports on dual-mode narrowband spectral selective detection are rather rare. The results of this work provide an exciting option for realizing bias-switchable dual-mode narrowband spectral selective detection in distinct bands by adjusting the polarity of the bias across the device. This technology has significant potential for a plethora of applications, including encrypted optical communication, bioimaging, security monitoring, self-aligned imaging in distinct bands, and miniaturized, portable, and non-invasive health monitoring systems.

In summary, we have successfully developed dual-mode narrowband OPDs for self-aligned imaging in the NIR-I and NIR-II regions, employing a CCN/photodiode double BHJ configuration. This design enables dual-mode narrowband spectral selectivity by strategically combining broadband absorbing materials. When operated under a forward bias, the front BHJ, enhanced by the CCN effect, exhibits a narrowband spectral response in the NIR-I range, with an FWHM of 38 nm and a *D** of 6×10^{11} Jones. In contrast, when under a reverse bias,

the OPD delivers narrowband spectral detection in the NIR-II range, with a responsivity of 50 mA/W. The bias-switchable dual-mode narrowband OPD provides a significant technical advantage for self-aligned imaging across distinct NIR-I and NIR-II bands, ensuring minimal spectral crosstalk. This capability paves the way for exciting applications in high-resolution bioimaging and secure optical communication, highlighting the potential of these OPDs in advanced technological fields.

Methods

Device fabrication

ITO-coated glass substrates with a sheet resistance of 10 Ω/sq were used for device fabrication. The ITO/glass substrates were cleaned by ultrasonication sequentially in detergent solution, deionized water, acetone, and isopropanol, each for 30 min. The ZnO nanoparticle solution was obtained from Sigma-Aldrich. The blend solution of PM6 (from eflexpv) and IT-4F (from Lumtec) was prepared by dissolving PM6 and IT-4F in chloroform (CF) with a weight ratio of 1:1, resulting in a concentration of 60 mg/ml. A 0.2 vol% 1,8-diiodooctane additive solution was added to the PM6:IT-4F (1:1) solution for device fabrication. The ternary functional layers were prepared using a blend solution of PTB7-Th (from 1-materials), COTIC-4Cl (from 1-materials), and Y6 (from eflexpv), formulated by dissolving PTB7-Th, COTIC-4Cl, and Y6 in CF solvent with a weight ratio of 1:1.05:0.45, resulting in a concentration of 40 mg/ml. A 2 vol% 1-chloronaphthalene solution was added to the ternary PTB7-Th:COTIC-4Cl:Y6 (1:1.05:0.45) blend solution for device fabrication.

A 10 nm thick ZnO electron-transporting layer (ETL) was deposited on the ITO/glass substrate by spin-coating at 2500 rpm for 50 s. A 3.5 μm thick PM6:IT-4F photoactive layer was formed on the ZnO ETL by spin-coating the PM6:IT-4F blend solution at 100 rpm for 50 s, followed by annealing at 100 °C for 10 min. The glass/ITO/ZnO/PM6:IT-4F samples were then transferred to an adjacent vacuum chamber with a base pressure of <4.0 × 10^{-4} Pa for depositing a 5 nm thick MoO$_3$ hole-transporting layer (HTL) by thermal evaporation. A 670 nm thick PTB7-Th:COTIC-4Cl:Y6 (1:1.05:0.45) photoactive layer spin-coated on the surface of a pre-cleaned silicon wafer, cleaned with acetone and isopropanol, each for 30 min. This layer was then transferred onto the surface of the ITO/ZnO/PM6:IT-4F/MoO$_3$ multilayer, forming a double BHJ configuration with the layer structure of glass/ITO/ZnO (10 nm)/PM6:IT-4F (3.5 μm)/MoO$_3$ (5 nm)/PTB7-Th:COTIC-4Cl:Y6 (670 nm). A 10 nm thick ZnO ETL was then deposited on the double BHJ stack by spin-coating at 2500 rpm for 50 s. Finally, a 100 nm thick Ag upper electrode was deposited on the ZnO ETL by thermal evaporation. The dual-mode narrowband OPDs have an active area of 3.0 mm × 3.0 mm, defined by the overlapping area between the front ITO and upper Ag contacts.

Device characterization

The responsivity of the OPDs was measured using a quantum efficiency measurement system comprising a xenon lamp (Zolix), a monochromator (Bentham TMc300), a Stanford Research System (SRS) preamplifier (model SR570), a chopper (SR540), and an SRS lock-in amplifier (model SR830). The *J*−*V* characteristics of the OPDs were measured using a source meter (Keithley 2400). The photocurrent for image analysis in the imaging measurement setup was measured using a preamplifier (model SR570) and a lock-in amplifier (model SR830).

Optical simulation

The distribution of optical density and absorption profile in the NIR-I and NIR-II dual-band narrowband OPDs was calculated using open-source software, a general-purpose photovoltaic device model (gpvdm), over the wavelength range from 350 to 1200 nm. The optical constants, including the wavelength-dependent refractive indexes, $n(\lambda)$, and extinction coefficients, $k(\lambda)$, of the photoactive layers PM6:IT-
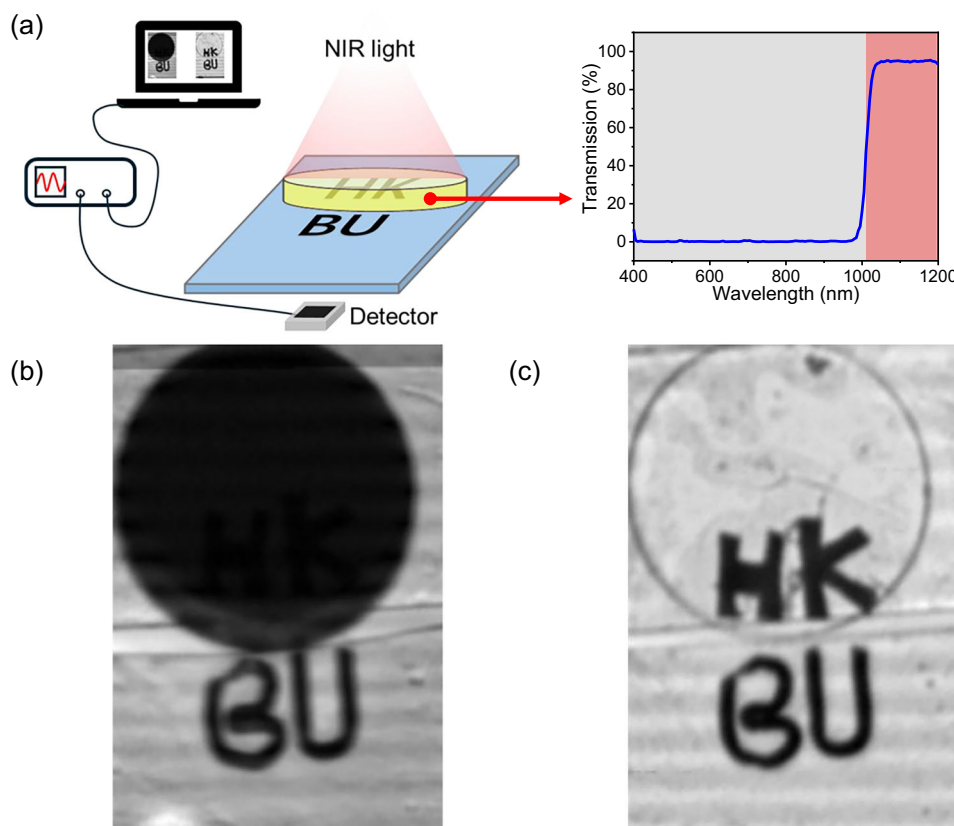
Fig. 6 | Self-aligned imaging in NIR-I and NIR-II. a Imaging measurement setup with a HKBU mask, where the upper part (e.g., the letters HK) is covered by a 1000 nm bandpass filter, used to demonstrate NIR-I and NIR-II selective detection using a dual-mode narrowband OPD. **b** Image showing only the BU part of the mask, produced by the OPD operated under a forward bias of 1.0 V. **c** The entire HKBU image produced by the OPD operated under a reverse bias of −1.0 V.

4F (1:1) and PTB7-Th:COTIC-4Cl:Y6 (1:1.05:0.45), as shown in Supplementary Fig. 7, were obtained by ellipsometry measurements.

Data availability
The data that support the findings of this study are presented in the main text and Supplementary Information file. All the data are available from the corresponding authors on request.

References

1. Khan, Y. et al. Organic multi-channel optoelectronic sensors for wearable health monitoring. *IEEE Access* **7**, 128114–128124 (2019).
2. Ring, E. F. & Ammer, K. Infrared thermal imaging in medicine. *Physiol. Meas.* **33**, R33–R46 (2012).
3. Xu, W., Wang, D. & Tang, B. Z. NIR-II AIEgens: a win-win integration towards bioapplications. *Angew. Chem. Int. Ed.* **60**, 7476–7487 (2021).
4. Tang, S., Chen, M. & Zheng, N. Multifunctional ultrasmall Pd nanosheets for enhanced near-infrared photothermal therapy and chemotherapy of cancer. *Nano Res.* **8**, 165–174 (2014).
5. Wang, Z., Tang, Y., Gao, M., Han, J. & Zhu, F. Advanced flexible organic near-infrared photodetectors for sensing applications. *Wearable Electron* **2**, 124–148 (2025).
6. Bhat, G. et al. Energy-level manipulation in novel indacenodithiophene-based donor-acceptor polymers for near-infrared organic photodetectors. *ACS Appl. Mater. Interfaces* **13**, 29866–29875 (2021).
7. Zheng, K. et al. Enhanced Near-infrared organic photodetectors leveraging core–shell nanotripods. *ACS Appl. Mater. Interfaces* **17**, 34304–34316 (2025).
8. Pu, K. et al. A flexible sensitive visible-NIR organic photodetector with high durability. *Adv. Mater. Technol.* **8**, 2300207 (2023).
9. Fuentes-Hernandez, C. et al. Large-area low-noise flexible organic photodiodes for detecting faint visible light. *Science* **370**, 698–701 (2020).
10. Lan, Z., Cai, L., Luo, D. & Zhu, F. Narrowband near-infrared perovskite/polymer hybrid photodetectors. *ACS Appl. Mater. Interfaces* **13**, 981–988 (2021).
11. Wang, Z., Tang, Y., Han, J. & Zhu, F. Visible-blind near-infrared organic photodetectors. *Appl. Phys. Lett.* **124**, 021103 (2024).
12. Lan, Z. et al. Filter-free band-selective organic photodetectors. *Adv. Opt. Mater.* **8**, 2001388 (2020).
13. Tang, Z. et al. Polymer: fullerene bimolecular crystals for near-infrared spectroscopic photodetectors. *Adv. Mater.* **29**, 1702184 (2017).
14. Siegmund, B. et al. Organic narrowband near-infrared photodetectors based on intermolecular charge-transfer absorption. *Nat. Commun.* **8**, 15421 (2017).
15. Kaiser, C. et al. Manipulating the charge transfer absorption for narrowband light detection in the near-infrared. *Chem. Mater.* **31**, 9325–9330 (2019).
16. Xing, S. et al. Miniaturized VIS-NIR spectrometers based on narrowband and tunable transmission cavity organic photodetectors with ultrahigh specific detectivity above 10(14). *Jones. Adv. Mater.* **33**, e2102967 (2021).
17. Yang, J. et al. Cavity-enhanced near-infrared organic photodetectors based on a conjugated polymer containing [1,2,5]selenadiazolo[3,4-c]pyridine. *Chem. Mater.* **33**, 5147–5155 (2021).
18. Zhao, Z. et al. Ultraviolet narrowband photomultiplication type organic photodetectors with Fabry–Pérot resonator architecture. *Adv. Funct. Mater.* **32**, 2203606 (2022).
19. Liu, M. et al. Ultra-narrow-band NIR photomultiplication organic photodetectors based on charge injection narrowing. *J. Phys. Chem. Lett.* **12**, 2937–2943 (2021).

20. Wang, W. et al. Organic photodetectors with gain and broadband/ narrowband response under top/bottom illumination conditions. *Adv. Opt. Mater.* **6**, 1800249 (2018).
21. Xie, B. et al. Self-filtering narrowband high performance organic photodetectors enabled by manipulating localized Frenkel exciton dissociation. *Nat. Commun.* **11**, 2871 (2020).
22. Lin, Q., Armin, A., Burn, P. L. & Meredith, P. Filterless narrowband visible photodetectors. *Nat. Photonics* **9**, 687–694 (2015).
23. Li, L. et al. Self-filtered narrowband perovskite photodetectors with ultrafast and tuned spectral response. *Adv. Opt. Mater.* **5**, 1700672 (2017).
24. Pecunia, V. Efficiency and spectral performance of narrowband organic and perovskite photodetectors: a cross-sectional review. *J. Phys Mater.* **2**, 042001 (2019).
25. Vanderspikken, J., Maes, W. & Vandewal, K. Wavelength-selective organic photodetectors. *Adv. Funct. Mater.* **31**, 2104060 (2021).
26. Lan, Z. et al. Dual-band organic photodetectors for dual-channel optical communications. *Laser Photonics Rev.* **16**, 2100602 (2022).
27. Tang, X., Ackerman, M. M., Chen, M. & Guyot-Sionnest, P. Dual-band infrared imaging using stacked colloidal quantum dot photodiodes. *Nat. Photonics* **13**, 277–282 (2019).
28. Lan, Z. et al. Near-infrared and visible light dual-mode organic photodetectors. *Sci. Adv.* **6**, eaaw8065 (2020).
29. Huang, W. T. et al. Near-infrared windows I and II phosphors for theranostic applications: spectroscopy, bioimaging, and light-emitting diode photobiomodulation. *Adv. Opt. Mater.* **11**, 2202061 (2022).
30. Luo, X., Chen, M. & Yang, Q. Research progress on near infrared II technology for in vivo imaging. *Acta Chim. Sin.* **78**, 373–381 (2020).
31. Chen, J. et al. A H_2O_2-activatable nanoprobe for diagnosing interstitial cystitis and liver ischemia-reperfusion injury via multispectral optoacoustic tomography and NIR-II fluorescent imaging. *Nat. Commun.* **12**, 6870 (2021).
32. Peumans, P., Yakimov, A. & Forrestb, S. R. Small molecular weight organic thin-film photodetectors and solar cells. *J. Appl. Phys.* **93**, 3693–3723 (2003).
33. Armin, A., Jansen-van Vuuren, R. D., Kopidakis, N., Burn, P. L. & Meredith, P. Narrowband light detection via internal quantum efficiency manipulation of organic photodiodes. *Nat. Commun.* **6**, 6343 (2015).
34. Yazmaciyan, A., Meredith, P. & Armin, A. Cavity enhanced organic photodiodes with charge collection narrowing. *Adv. Opt. Mater.* **7**, 1801543 (2019).
35. Liu, Q. et al. Electron-donating amine-interlayer induced n-type doping of polymer:nonfullerene blends for efficient narrowband near-infrared photo-detection. *Nat. Commun.* **13**, 5194 (2022).
36. Fang, Y., Armin, A., Meredith, P. & Huang, J. Accurate characterization of next-generation thin-film photodetectors. *Nat. Photonics* **13**, 1–4 (2018).
37. Lan, Z., Lee, M.-H. & Zhu, F. Recent advances in solution-processable organic photodetectors and applications in flexible electronics. *Adv. Intell. Syst.* **4**, 210016 (2021).
38. Simone, G., Dyson, M. J., Meskers, S. C. J., Janssen, R. A. J. & Gelinck, G. H. Organic photodetectors and their application in large area and flexible image sensors: the role of dark current. *Adv. Funct. Mater.* **30**, 1904205 (2019).
39. Bao, C. et al. Low-noise and large-linear-dynamic-range photodetectors based on hybrid-perovskite thin-single-crystals. *Adv. Mater.* **29**, 1703209 (2017).
40. Wu, Z., Zhai, Y., Kim, H., Azoulay, J. D. & Ng, T. N. Emerging design and characterization guidelines for polymer-based infrared photodetectors. *Acc. Chem. Res.* **51**, 3144–3153 (2018).
41. Wu, Z., Yao, W., London, A. E., Azoulay, J. D. & Ng, T. N. Elucidating the detectivity limits in shortwave infrared organic photodiodes. *Adv. Funct. Mater.* **28**, 1800391 (2018).
42. Lee, M., Lan, Z. & Zhu, F. Recent advances in solution-processable organic photodetectors and applications in flexible electronics. *Adv. Intell. Syst.* **4**, 2100167 (2022).

Acknowledgements

Author contributions

F.Z. supervised the execution of the project. Y.T. conceived this project and designed the experiments, and fabricated the devices. Z.W. measured the spectral response performances of the devices. M.G. conducted the NIR imaging measurement. J.H. and L.Y. performed optical simulations and analyses. Y.T. and F.Z. drafted and finalized the manuscript. All authors participated in the discussions for manuscript preparation.

Competing interests

The authors declare no competing interests.

Additional information

Supplementary information The online version contains supplementary material available at https://doi.org/10.1038/s41467-025-62394-6.

Correspondence and requests for materials should be addressed to Furong Zhu.

Peer review information *Nature Communications* thanks the anonymous reviewer(s) for their contribution to the peer review of this work. A peer review file is available.

Reprints and permissions information is available at http://www.nature.com/reprints

Publisher's note Springer Nature remains neutral with regard to jurisdictional claims in published maps and institutional affiliations.